NeuroImage 203 (2019) 116163

Contents lists available at ScienceDirect

NeuroImage

journal homepage: www.elsevier.com/locate/neuroimage

A population stereotaxic positron emission tomography brain template for the macaque and its application to ischemic model

Binbin Nie [a,1], Lu Wang [b,1], Yichao Hu [c], Shengxiang Liang [a], Zhiqiang Tan [b], Pei Chai [a], Yongjin Tang [b], Jingjie Shang [b], Zhangsheng Pan [b], Xudong Zhao [d], Xiaofei Zhang [e], Jianxian Gong [f], Chao Zheng [g], Hao Xu [b,*], Hsiao-Ying Wey [g], Steven H. Liang [e], Baoci Shan [a,b,h,**]

[a] Beijing Engineering Research Center of Radiographic Techniques and Equipment, Institute of High Energy Physics, Chinese Academy of Sciences & School of Nuclear Science and Technology, University of Chinese Academy of Sciences, Beijing, 100049, China
[b] Department of Nuclear Medicine and PET/CT-MRI Center, The First Affiliated Hospital of Jinan University & Institute of Molecular and Functional Imaging, Jinan University, Guangzhou, 510630, China
[c] College of Information Engineering, Xiangtan University, Xiangtan, 411105, China
[d] Institute of Biophysics, Chinese Academy of Sciences, Beijing, 100101, China
[e] Division of Nuclear Medicine and Molecular Imaging, Massachusetts General Hospital & Department of Radiology, Harvard Medical School, Boston, MA, 02114, USA
[f] State Key Laboratory of Chemical Oncogenomics, Key Laboratory of Chemical Genomics, Peking University Shenzhen Graduate School, Shenzhen, 518055, China
[g] Athinoula A. Martinos Center for Biomedical Imaging, Department of Radiology, Massachusetts General Hospital, Harvard Medical School, Charlestown, MA, 02129, USA
[h] CAS Center for Excellence in Brain Science and Intelligence Technology, Shanghai, 200031, China

ARTICLE INFO

Keywords:
Positron emission tomography
PET
Macaque
Brain
MRI
Template
Ischemia

ABSTRACT

Purpose: Positron emission tomography (PET) is a non-invasive imaging tool for the evaluation of brain function and neuronal activity in normal and diseased conditions with high sensitivity. The macaque monkey serves as a valuable model system in the field of translational medicine, for its phylogenetic proximity to man. To translation of non-human primate neuro-PET studies, an effective and objective data analysis platform for neuro-PET studies is needed.

Materials and methods: A set of stereotaxic templates of macaque brain, namely the Institute of High Energy Physics & Jinan University Macaque Template (HJT), was constructed by iteratively registration and averaging, based on 30 healthy rhesus monkeys. A brain atlas image was created in HJT space by combining sub-anatomical regions and defining new 88 bilateral functional regions, in which a unique integer was assigned for each sub-anatomical region.

Results: The HJT comprised a structural MRI T1 weighted image (T1WI) template image, a functional FDG-PET template image, intracranial tissue segmentations accompanied with a digital macaque brain atlas image. It is compatible with various commercially available software tools, such as SPM and PMOD. Data analysis was performed on a stroke model compared with a group of healthy controls to demonstrate the usage of HJT.

Conclusion: We have constructed a stereotaxic template set of macaque brain named HJT, which standardizes macaque neuroimaging data analysis, supports novel radiotracer development and facilitates translational neuro-disorders research.

1. Introduction

Owing to the phylogenetic proximity to human, the macaque monkey (rhesus and cynomolgus) has been served as a valuable model system in the field of translational medicine (Zhang and Shi, 1993). Complementary to human brain studies, investigations into the functional and molecular information of macaque brain via non-invasive imaging technologies facilitate our understanding of the central nervous system,

* Corresponding author.
** Corresponding author. Beijing Engineering Research Center of Radiographic Techniques and Equipment, Institute of High Energy Physics, Chinese Academy of Sciences & School of Nuclear Science and Technology, University of Chinese Academy of Sciences, Beijing, 100049, China.
E-mail addresses: txh@jnu.edu.cn (H. Xu), shanbc@ihep.ac.cn (B. Shan).
[1] These two authors contributed equally to this work.

https://doi.org/10.1016/j.neuroimage.2019.116163
Received 29 April 2019; Received in revised form 3 July 2019; Accepted 3 September 2019
Available online 5 September 2019

contribute to pathogenesis research and accelerate drug development. Positron emission tomography (PET) is a non-invasive in vivo imaging technology that is commonly used in basic research and clinical trials. With the assistance of PET radiotracers and the structural information provided by magnetic resonance imaging (MRI), PET imaging can help us evaluate brain function and neuronal activity in normal and diseased conditions with high sensitivity. Therefore, it is necessary to develop an efficient data analysis method for macaque neuroimaging, which could facilitate better understanding of translational benefits from non-human primate (NHP).

To make precise inference and interpretation of neuroimaging results, a predefined imaging modality template, is requisite in both voxel- and region-of-interest (ROI)-based neuroimaging data analysis. When neuroimaging data from each subject is typically transformed into a common space, such as the Montreal Neurological Institute (MNI) template space (Mazziotta et al., 2001), group comparisons and longitudinal tracking across time could be performed. Moreover, ROIs in template space could be extracted automatically and objectively (Tzourio-Mazoyer et al., 2002). A population brain template, usually derived from multiple individuals imaging data, has been proved to be an accurate, reproducible and consistent tool for analysis and comparison of functional brain images since it has greater cross-subject validity via increasing statistical power (Friston et al., 1999).

In past decades, several structural MRI brain templates of macaque with high spatial resolution have been developed (Black et al., 2004; McLaren et al., 2009; Quallo et al., 2010; Frey et al., 2011; Van Essen et al., 2012; Seidlitz et al., 2018; Rohlfing et al., 2012). Although the PET images could be normalized via the corresponding MRI T1 weighted image (T1WI) structural template (which called MRI-aided registration), many imaging studies have demonstrated that the normalization accuracy has been substantially improved when registering the individual PET images to the same modality PET template (Collantes et al., 2009; Chae et al., 2014). For instance, in human brain studies, PET template images with different radiotracers have been constructed, such as Tau-PET template, D2-receptor PET template, as well as [^{18}F]fludeoxyglucose (FDG)-PET template (Meyer et al., 1999) which was derived from 152 subjects in MNI space. However, in NHP research, because only a limited number of sample sets was used in an FDG-PET template (six health rhesus macaques) (Cross et al., 2000) and dopamine receptor PET template (eleven cynomolgus macaques) (Collantes et al., 2009), it is still imperative to construct a population PET template image from a large cohort of macaques to facilitate brain studies in NHP. In addition, since different radiotracers have different image intensity distributions, frequently, in the specific receptor PET imaging studies, the MRI-aided registration method is always used (Cho et al., 2016; Chiotis et al., 2018), Serving as a bridge between the receptor images and the common template space, is always used. Therefore, a new macaque brain MRI template with an approximate spatial resolution to PET images is highly beneficial.

In this study, a large cohort of rhesus macaques underwent PET and MRI scans, and then iteratively registered and averaged using a validated template-creation process (Mazziotta et al., 2001; Friston et al., 1999; Nie et al., 2013, 2014, 2019; Liang et al., 2017; Huang et al., 2018). The resulting template, namely, the Institute of High Energy Physics & Jinan University Macaque Template (HJT) mainly contains four parts: (1) the population T1WI structural template, which is mainly used for MRI-aided normalization in the receptor or new radiotracers PET imaging studies; (2) the population FDG-PET functional template, which is mainly used for FDG-PET studies; (3) a set of tissue probability maps (TPM), which is mainly used for tissue segmentation; (4) a functional atlas image, which is mainly used for sub-functional regions segmentation. The constructed HJT also shared a same coordinate space with the *D99-SL* template (Reveley et al., 2017), so that sub-anatomical segmentation could be automatically applied. To improve the visualization of neuroimaging data analysis, HJT surfaces were also constructed. As proof-of-concept, we have successfully demonstrated the spatial normalization capability of HJT using FDG-PET data obtained from different PET centers. Single-subject voxel-wised analysis has been performed on an ischemic monkey model (Chen et al., 2015a) and a group of healthy controls, demonstrating the usage and accuracy of HJT.

Our constructed HJT is packed in a commonly used NIFTI format, which is compatible with many commercially available software tools, such as Statistical Parametric Mapping (SPM) and PMOD (https://www.pmod.com/web/). Furthermore, the HJT volume, segmentations, and surface representations in HJT will be openly available to the research community (see Supporting Information). This package will demonstrate a standardized macaque brain coordinate system for localizing any spatial neuroimaging data and rationalizing both single- and multi-subject hybrid PET/MRI data analysis, which is beneficial for cross-animal imaging comparative studies.

2. Material and methods

2.1. Subject information

For HJT construction, a number of healthy rhesus macaques (*Macaca mulatta*) were used for MRI scan. Two experienced veterinary staff evaluated and confirmed the health condition of the monkey, and among them, 30 healthy rhesus monkeys were selected for neuroimaging data collection. The monkeys were young and adults between 5 and 12 years old when scanned (average of 7.9 years). The ages of the 21 females and nine males were comparable (7.7 ± 2.3 and 8.4 ± 1.5 years, respectively). The monkeys weighed 7.0 kg on average at the time of scan collection, with the males weighing slightly more than the females on average (8.1 ± 1.1 vs. 6.6 ± 1.5 kg). All of these 30 rhesus monkeys were also used for FDG-PET imaging (Table S1). None of these monkeys used in this study had undergone an invasive brain procedure (e.g., craniotomy).

To evaluate the compatibility of HJT for processing neuro-PET data from different sub-species of monkeys, different site/scanner and neurologic disease model, 1 rhesus macaque (male, 10 years, 8.0 kg), 1 cynomolgus monkey (female, 3 years, 2.7 kg) and 1 ischemic stroke cynomolgus model (male, 8 years, 7.5 kg) were also used for FDG-PET data collection (Table S2). Furthermore, another ten healthy cynomolgus macaques (male, 7.3 ± 5.6 years, 5.2 ± 2.7 kg) received FDG-PET/CT brain scans; the data were used as a control group for single-subject voxel-wised analysis of the index of glucose metabolism in stroke model brain (Table S3).

The flowchart for HJT construction, evaluation, and the application was summarized in Supplementary Scheme S1.

The research protocol for the macaque neuroimaging study was approved by the Laboratory Animal Ethics Committee, Jinan University and its collaborative animal facility (Guangzhou), and/or Animal Care and Use Committee of the Chinese Academy of Sciences (Beijing), China.

2.2. Data acquisition

2.2.1. MRI data acquisition

T1-weighted MR anatomical images were acquired on a 3.0 T scanner (GE Discovery 750, Milwaukee, USA) at the PET/CT-MRI center in the First Affiliated Hospital of Jinan University.

Each macaque was anesthetized with ketamine (10 mg/kg; intramuscular injection) and placed into the scanner in the supine position. A circular 32-channel array head coil was placed on top of the monkey's head. The whole-brain images were acquired with a 3D Bravo T1 sequence (TR = 8.4 ms, TE = 3.4 ms, TI = 450 ms, slice thickness = 1.1 mm, matrix size = 256 × 256, FOV = 18 × 18 cm). Each scan was acquired within 10 min.

2.2.2. PET data acquisition

Forty-two macaques were scanned on a PET/CT system (GE Discovery Elite 690, USA, Spatial Resolution 4–5 mm) at the PET/CT-MRI center in

the First Affiliated Hospital of Jinan University in Guangzhou, including the 30 healthy rhesus macaques, 11 healthy cynomolgus and one ischemic stroke model. Another rhesus, from Primate Research Center, State Key Laboratory of Brain and Cognitive Science, was scanned at the Institute of High Energy Physics (IHEP) in Beijing with an animal PET system (E-plus260, IHEP, CAS, China, Spatial Resolution ~ 2.0 mm) (Chai et al., 2019). FDG was obtained from Guangzhou HTA Co., Ltd and Beijing HTA Co., Ltd, respectively, with high quality.

All the monkeys were deprived of food for 12–15 h before FDG injection, but allowed to drink water at any time. Each monkey was intravenously injected 0.7–0.9 mL of FDG (18.5 MBq/1000 g of body weight) while awake, then kept with minimal ambient noise and light in an isolated and shielded area. After 50 min, the macaque was anesthetized with ketamine (10 mg/kg; i.m.), placed into the scanner, and maintained in light narcosis with 2% isoflurane and 98% oxygen. Head position was fixed with a stereotactic frame. The body of the subject was in the supine position.

Protocols in Guangzhou: CT scan was performed firstly, followed by an 8-min static positron emission data collection at 60 min post-injection. CT data were acquired for attenuation-corrections. PET data were collected with a slice thickness of 3.27 mm, slice interval of 3.75 mm, matrix size of 256 × 256 and scan FOV of 70 cm in 3D time-of-flight (TOF) mode. The CT data were reconstructed in standard mode with DFOV of 30 cm and window width/window level 100/45, advanced statistical iterative reconstruction 40%. The PET data were attenuation-corrected by integrated CTAC technology. In addition, in this study, we used the SharpIR algorithm, developed by GE Healthcare, which incorporated the point spread function (PSF) correction at sinogram level followed the method established by Alessio et al., in 2006 (Alessio et al., 2006). In practice, a fixe measurement for radical and axial detector response was taken, normalized and mapped to a model for every sinogram element. A detector matrix was achieved when this modeling process was done for the entire detector space, which was then incorporated into the reconstruction method (Rapisarda et al., 2010). Thus, the PET data were then reconstructed in terms of the point spread function (PSF) together with TOF technology with DFOV of 30 cm.

Protocols in Beijing: the Eplus-260 animal PET system has axial FOV of 64 mm and transverse FOV of 190 mm, with a spatial resolution of 1.5 mm at CFOV. The rhesus macaque was scanned on this system for two animal bed positions with 10 min for each bed position. Data were acquired in full 3D acquisition mode with a slice thickness of 1.0 mm. Corrections including decay, dead time, random, normalization, and

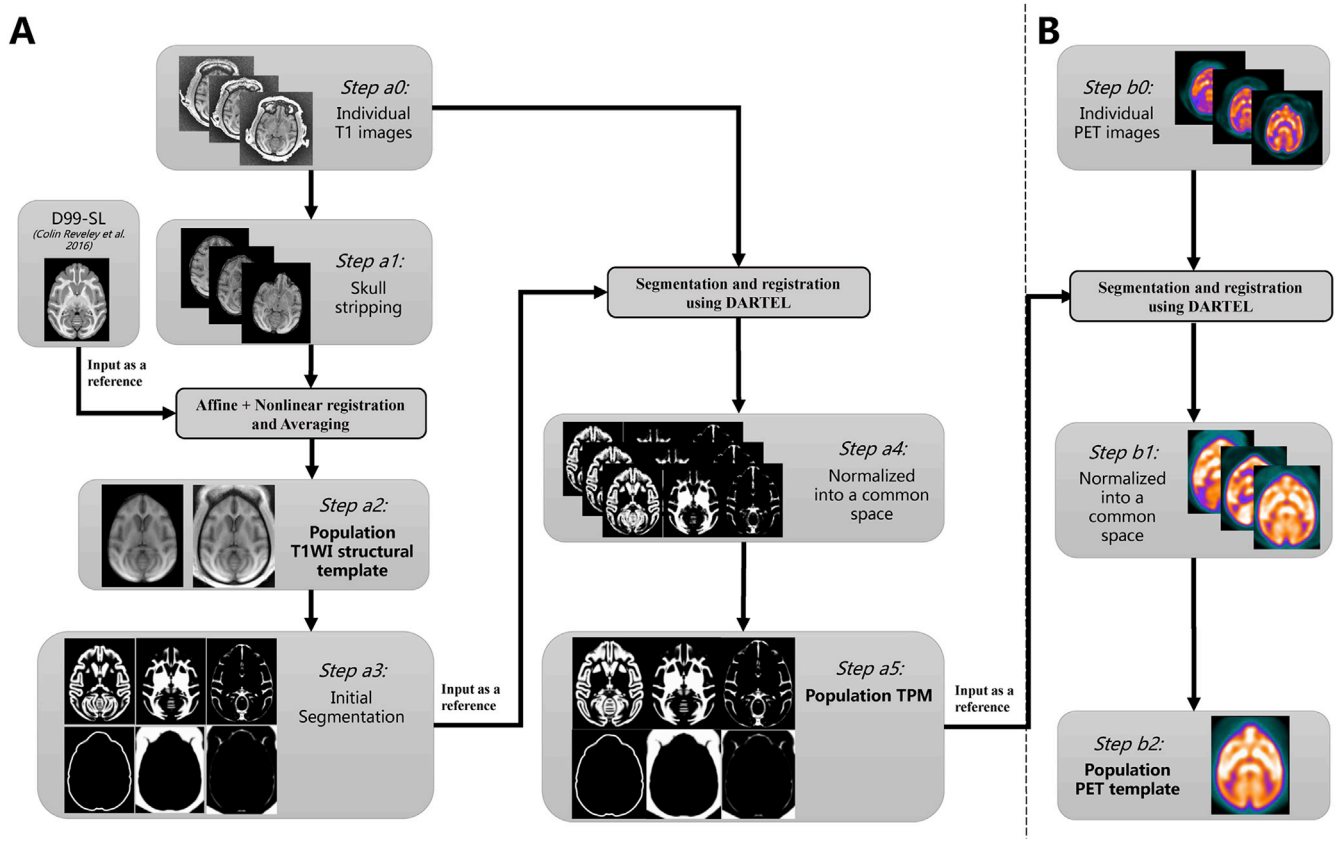

Fig. 1. Flow chart for creating population HJT in Saleem and Logothetis atlas space (2012), comprising (A) a T1WI structural template and a set of TPM, and (B) an FDG-PET functional template. Step a0: T1-weighted MRI scans were collected from 30 macaque monkeys in vivo. Step a1: These anatomical images were skull striped using Brain Extraction Tool (BET). Step a2: All these intracranial images were spatially normalized into a common space defined by *D99*-SL template in Saleem and Logothetis atlas space (2012), and carried their corresponding original T1WI structural images along. These normalized images were averaged to create a mean T1WI structural image. Using this mean T1WI image as a new reference, all the individual images were registered and averaged recursively, until the SD between two adjacent mean T1WI images is less than 5%. The latest mean T1WI image is accepted as the final population T1WI structural template. Step a3: This T1WI template was initially segmented into six tissue class maps based on image intensity using FSL (FMRIB Software Library), comprising three intracranial tissue classes - GM, WM and CSF, and three extracranial parts - skull, extracranial soft tissues and background. Step a4: Using this initial segmentation as a reference, all the 30 individual T1WI images were segmented and normalized by DARTEL algorithm in SPM12. Step a5: These normalized tissue class maps were averaged and regularized to create a mean TPM. Step a4 and Step a5 were executed recursively until the SD between two adjacent mean TPM is less than 5%. The latest TPM was accepted as the final population TPM. This population TPM was further used as a reference template in the construction of population FDG-PET template image. Step b0: FDG-PET images were collected from 25 macaque monkeys in vivo. Step b1: These functional images were normalized into the Saleem and Logothetis atlas space via the TPM created in Step a3, using DARTEL algorithm in SPM12. Step b2: The population FDG-PET template was finally created by averaging from these normalized FDG-PET images.

scatter corrections were applied. Attenuation is corrected based on the image segmentation method (Chai et al., 2019). Data were reconstructed using OSEM-PSF (4 iterations, subsets 12) algorithm, with a matrix size of 380 × 380 and a pixel size of 0.5 × 0.5 mm^2.

2.3. Construction of the population HJT

The flowchart for establishing population HJT is shown in Fig. 1. The HJT comprised a population T1W structural template image, a set of population TPM, and a population FDG-PET functional template image.

2.3.1. Construction of a population T1WI structural template in HJT

As shown in Fig. 1A, all these 30 T1WI structural images of rhesus brain were firstly semi-automatically skull stripped using Brain Extraction Tool (BET) (Popescu et al., 2012) in FSL (FMRIB Software Library) (*Step a1*) and then manually corrected. Then a population T1WI structural template in HJT was created recursively by spatially registering and averaging (*Step a2*). In detail, all these intracranial images were spatially normalized into a common space defined by *D99-SL* (Reveley et al., 2017) in *Saleem and Logothetis atlas* space (Saleem and Logothetis, 2012), using 12-parameter affine transformation and then non-linear registration method, and carried their corresponding original T1WI structural images. Then, a new reference image was created by averaging these normalized intracranial images. Based on this new reference image, all the original images were normalized and averaged iteratively. When the mean standard residual difference (SD) between two adjacent averaged images is less than 5% (Nie et al., 2013, 2019; Huang et al., 2018), the iteration is stopped. Finally, the latest mean image is accepted as the final population T1WI structural template, as shown in Fig. 2A.

2.3.2. Construction of a set population TPM in HJT

As shown in Fig. 1A, firstly, the constructed T1WI structural template in *Step a2* was initially segmented into six types based on image intensity using FSL. These six parts comprise the gray matter (*GM*), the white matter (*WM*), the cerebrospinal fluid (*CSF*), skull, extracranial soft tissues and background (*Step a3*). These six segmentations in HJT space were then saved as a 4D mask image.

Then the population TPM of macaque was created iteratively by tissue segmentation, registering and averaging in SPM12 (Friston, 1995) (*Step a4* and *Step a5*). In detail, using this initial segmentation as a reference (*Step a3*), all the 30 original T1WI images were segmented and normalized by the diffeomorphic anatomical registration through exponentiated lie (DARTEL) algorithm (Mak et al., 2011) (*Step a4*). Then, these normalized tissue class maps were averaged and regularized to create a mean 4D-TPM and selected as a new reference (*Step a5*). All the 30 original T1WI images were segmented, registered, averaged and regularized iteratively. Finally, when the SD between two adjacent *GM* of mean TPM is less than 5%, the latest mean 4D-TPM is accepted as the final population TPM in HJT, of which the intracranial tissue class maps were shown in Fig. 3.

2.3.3. Construction of a population FDG-PET functional template in HJT

Using the constructed population TPM as a reference input, each individual FDG-PET image was normalized into the HJT space by DARTEL (Mak et al., 2011) in SPM12 (*Step b1*). A new reference FDG-PET image was created by averaging these normalized FDG-PET images. Based on this new reference image, all these original FDG-PET images were normalized and averaged iteratively, until the SD between two adjacent mean FDG-PET images is less than 5%. The latest mean FDG-PET image is accepted as the final population FDG-PET functional template (*Step b2*), as shown in Fig. 2B.

Finally, to facilitate seamless integration with previous work, we maintained a similar coordinate space as the *D99-SL template* (Reveley et al., 2017) and the NMT template (Seidlitz et al., 2018). The origin of HJT is located at the center of the anterior commissure. The grid is organized with RAI ('Neurological') index order, in which the x-axis stands for medial-to-lateral, the y-axis stands for anterior-to-posterior (AP), and the z-axis stands for superior-to-inferior (SI).

2.4. Construction of sub-functional regions segmentation of the HJT

Our established HJT shares a similar coordinate space with the *D99-*

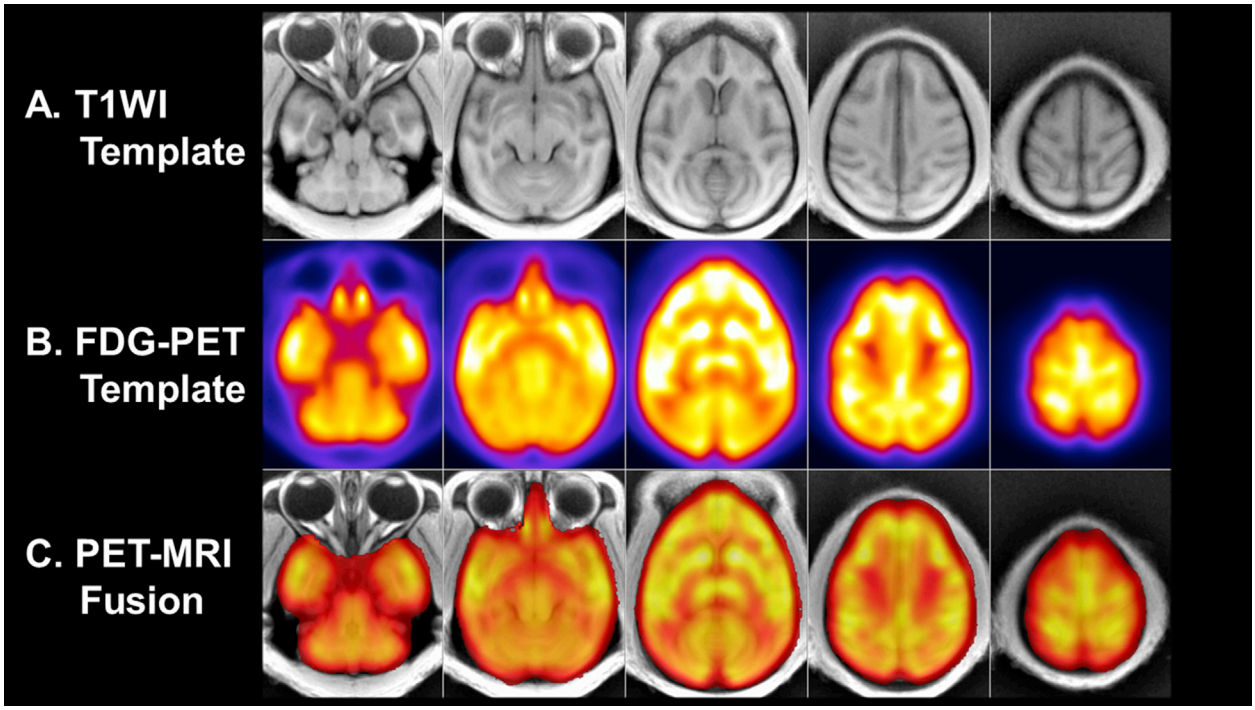

Fig. 2. Axial slices of the HJT. (A) Whole head anatomical T1WI template image. (B) Whole head functional FDG-PET template image. (C) Superimposing the intracranial FDG-PET template on the whole head T1WI anatomical template image. The functional images were presented in warm color, while the anatomical images were presented in gray-scaled as background.

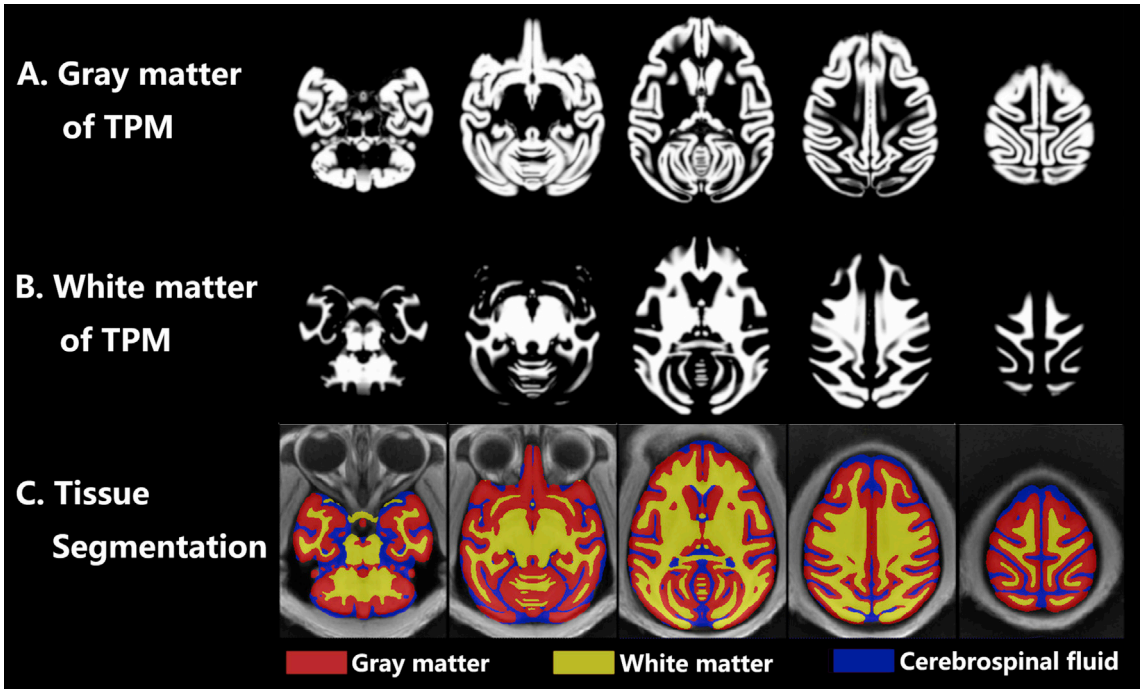

Fig. 3. Axial slices of intracranial tissue segmentation of HJT. (A) The gray matter of TPM. (B) The white matter of TPM. (C) Superimposing the intracranial tissue class segmentations on the whole head T1WI anatomical template image. The intracranial tissue segmentations were presented in pseudo-color (gray matter, red; white matter, yellow; cerebrospinal fluid, blue), while the anatomical images were presented in gray-scaled as background.

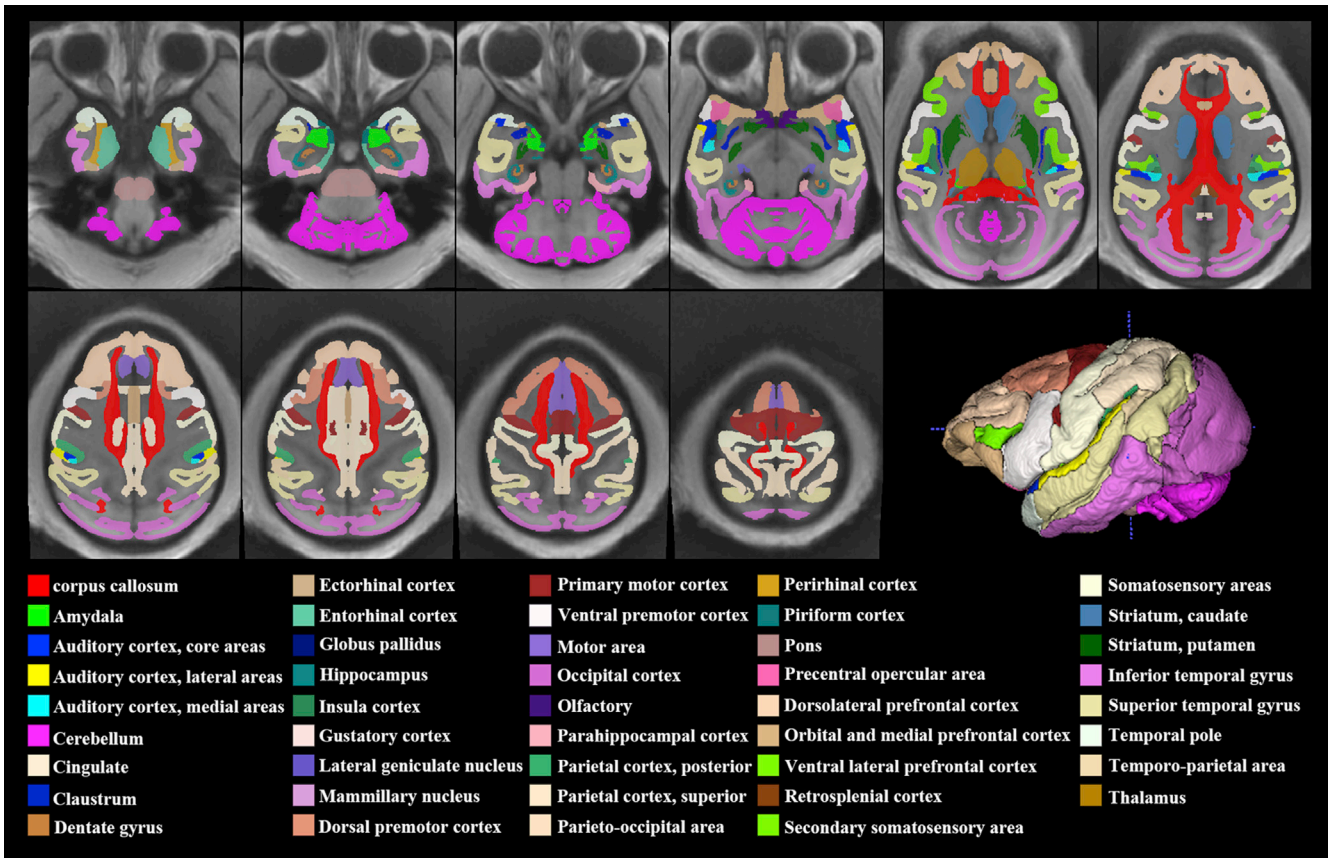

Fig. 4. Axial slices and a 3D rendering of sub-functional region segmentations of HJT. The sub-functional region segmentations were presented in pseudo-color, while the structural slices of HJT were presented in gray-scaled as background. Detailed information of these sub-functional regions was listed on the bottom panel, comprising pseudo color and name.

SL (Reveley et al., 2017), which would be beneficial to extracting ROI automatically from the fine delineations of sub-anatomical brain regions. Given the intrinsic spatial resolution of PET images, these fine delineated sub-anatomical regions (Saleem and Logothetis, 2012) were further combined according to their functions by an anatomist and a co-author (S.L.) in this study. Moreover, according to previous PET studies (Wang et al., 2016; Cheng et al., 2018), several commonly used regions were newly defined, such as thalamus, pons, caudate, putamen and corpus callosum. Finally, 44 functional regions were demonstrated. A new set of integer indices was assigned to these 44 functional regions as shown in Fig. 4. Odd/even integers were assigned for right/left corresponding functional regions to preserve laterality information.

2.5. HJT surface construction

The HJT surface was constructed from the population TPM mainly for viewing the statistical results in 3D space. In detail, the GM of the TPM was extracted and saved as a mask image. It was then segmented into left and right hemispheres halves, respectively. All these three mask images were saved as a render surface file. The full view of HJT surface is depicted in Fig. 5. By doing this, the significant regions, generated by voxel-wised or ROI-based analyses, could be mapped onto this brain surface with popular surface-based tools, such as the BrainNet View toolkit (http://www.nitrc.org/projects/bnv/) (Xia et al., 2013).

2.6. Application the constructed template set in stroke studies

With the assistance of HJT, a single-subject voxel-wised analysis was performed for analyzing an ischemic stroke cynomolgus macaque (Chen et al., 2015a) and ten healthy cynomolgus controls voxel-by-voxel on the platform of SPM12. Briefly, all the FDG-PET images from the ischemic model and controls were normalized into the HJT space via our constructed FDG-PET template using affine and nonlinear transformations. They were then resliced to $1 \times 1 \times 1\ mm^3$. These images were smoothed by a Gaussian kernel with a full width half maximum (FWHM) of $2 \times 2 \times 2\ mm^3$.

These preprocessed images were then conducted voxel-wised analysis based on the framework of the general linear model (GLM) in SPM12. In order to identify the differences of FDG signals between this ischemic stroke cynomolgus macaque and healthy controls, a two-sample *t*-test was performed. To account for global confounds, an unbiased scale factor was constructed and proportional scaling and intensity normalization were applied (Nie et al., 2018). Finally, brain regions with significant FDG changes were identified using $p < 0.05$ (FDR corrected) for voxel intensities and 20 voxels for cluster-extent.

2.7. An FDG metabolic functional network construction

There are two critical elements in network construction, the node and the edge. In HJT, the node could be defined easily by the functional atlas image. The edge could be defined by calculating the correlation of the FDG signal fluctuation. Therefore, we could conclude that the metabolic functional network of macaque could be established easily based on the HJT.

As an application example, a metabolic functional network was constructed from the FDG-PET images of the 30 healthy macaques in Gretna software (Wang et al., 2015). In this study, all the bilateral functional regions defined in the functional atlas of HJT, 82 brain regions (excluding the thalamus, corpus callosum and pons), were selected as the network node. The SUVR of each region were extracted from these 30 healthy macaques, in which the unbiased scale factor was selected as the reference (Nie et al., 2018). The Pearson's correlations were calculated between each pair of the regions. The correlation coefficient is regarded as network connections. Finally, the metabolic functional network was sparse and segmented into four modularity using the Greedy algorithm (Zhang et al., 2019).

3. Results

3.1. Constructed HJT and tissue segmentations

Our constructed stereotaxic brain template set of macaques named HJT is shown in Figs. 2 and 3 and available upon request. The population T1WI structural template image is shown in gray-scaled in Fig. 2A with a voxel size of $0.5 \times 0.5 \times 0.5\ mm^3$. The population FDG-PET functional template image is shown in pseudo-color in Fig. 2B with a voxel size of $1 \times 1 \times 1\ mm^3$. The intracranial segmentation of the constructed population FDG-PET functional template is presented with pseudo-color and superimposed on the T1WI template, as shown in Fig. 2C. The population intracranial TPM is shown in Fig. 3, in which the *GM*, *WM* and *CSF* are

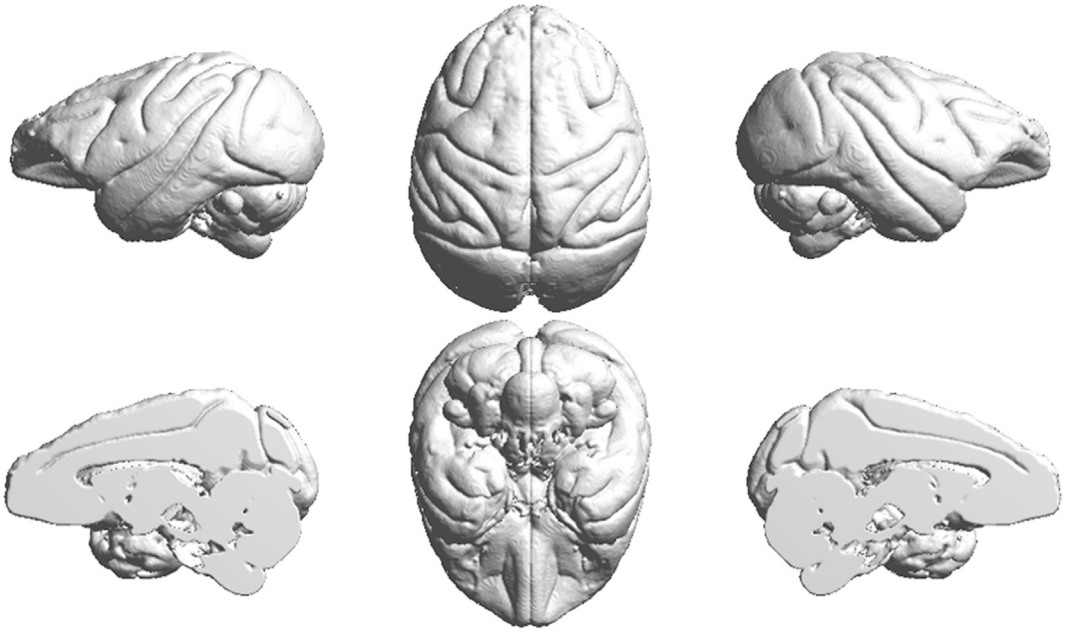

Fig. 5. The constructed HJT surface, which is compatible with other surface-based tools.

shown in red, yellow and blue, respectively (Fig. 3C). As illustrated in Figs. 2 and 3, the HJT set shares a common space.

3.2. Sub-functional regions segmentation of the HJT

In the process of neuroimaging data based on either voxel- or ROI-based approaches, an automatic and accurate sub-anatomical segmentation improves the accuracy, reproducibility and consistency. Recently, two MRI brain structural templates of macaque named *D99-SL* (Reveley et al., 2017) and NMT (Seidlitz et al., 2018) have been established, and accompanied with a fine sub-anatomical delineated digital atlas image in *Saleem and Logothetis atlas* (Saleem and Logothetis, 2012) space, in which hundreds of them have been delineated. Considering the spatial resolution of PET imaging, the digital macaque brain regions were re-combined and further defined in this work, generating a new functional macaque brain atlas which contains 44 sub-functional regions. These sub-functional regions are commonly used in PET imaging studies, such as analysis of brain tissue time-activity curve of the radiotracer, and computation of SUVR with specific brain region (*i.e.* cerebellum, white matter, pons) as a reference (Chen et al., 2015b). The alignment of our constructed template set to the digital anatomical atlas is shown in Fig. 4. This digital functional atlas image is shown in color-scaled, and superimposed on the structural slices and 3D render of HJT. Detailed information of these sub-functional regions was listed on the bottom panel, comprising pseudo color and name. As illustrated, there is a high degree of alignment between the atlas areas and HJT.

3.3. Constructed HJT surface

The constructed HJT surface is shown in Fig. 5, with details in the left/right lateral view, the top/bottom dorsal view and the left/right vertical section view. This surface is compatible with other popular surface-based tools, such as the BrainNet View (Xia et al., 2013). It can be used for viewing one or more sub-functional regions on a 3D render surface. Furthermore, voxel-wised statistical results can also be overlaid and saved as a picture (Fig. 7) or a movie (Supplementary movie). All these views of the HJT surface could be used either simultaneously or separately for different purposes.

3.4. Evaluation and application of the HJT

3.4.1. Spatial normalization of FDG-PET images

All the individual images are initially normalized into a standardized space prior to statistical analysis, which is a critical step in PET data analysis. To demonstrate the spatial normalization capability of HJT, three FDG-PET data sets were used (Table S2), which were obtained from different imaging centers and different subtypes of macaque. All these FDG-PET images were normalized into the HJT space via the FDG-PET template using affine and nonlinear transformations. The normalization results were shown in Fig. 6, comprising with a healthy rhesus macaque from IHEP cohort (Fig. 6A), a healthy cynomolgus macaque (Fig. 6B) and a stroke model cynomolgus (Fig. 6C) from JNU cohort. These original FDG-PET images (first column) can be normalized into the HJT space directly, without time-consuming and labor-intensive skull stripping by manually methods. After spatial normalization (second column), the skull is stripped (third column) directly using the intracranial mask image of HJT. Moreover, different tissue classes are segmented using the TPM of HJT, such as the gray matter (fourth column). All the sub-functional regions of interest can also be extracted easily using the atlas of HJT, such as the striatum (fifth column).

To quantitatively evaluate the spatial normalization result, the Dice similarity coefficient (DS_c) (Gutierrez and Zaidi, 2012) was calculated between the ten normalized healthy cynomolgus macaques (IM_{indi}) and the constructed FDG-PET template image (IM_{temp}). The DS_c is the volume overlap metric which quantifies the intersection between the template and normalized individual by their mean volume (the excellent agreement value is >80%) as in Eq. (1).

$$DS_c = 2 \times \frac{IM_{indi} \cap IM_{temp}}{IM_{indi} + IM_{temp}} \quad (1)$$

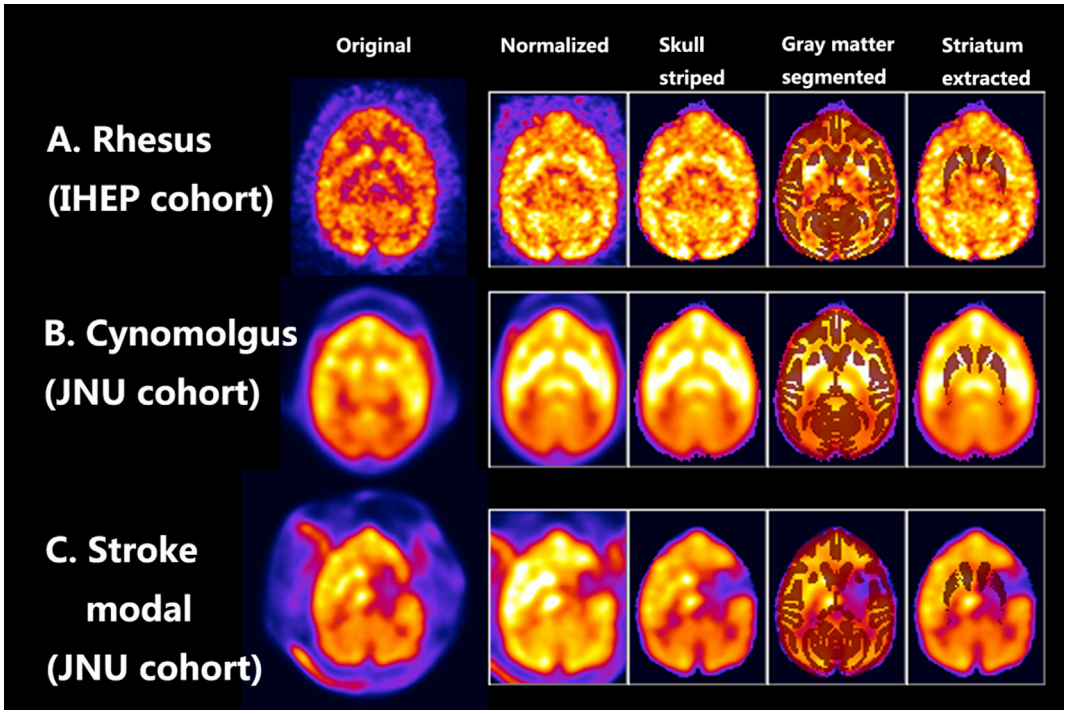

Fig. 6. Qualitative evaluation of the efficiency for spatial normalization based on HJT. One axial slice of three example macaques from different cohorts were demonstrated, including one healthy rhesus from IHEP, one healthy cynomolgus and one stroke modal from JNU. All these original images were normalized into the HJT space according the FDG-PET template. Then, the skull could be striped automatically by the intracranial mask. The tissue classes could be separated according to the TPM, such as the gray matter. Moreover, any sub-anatomical region could be segmented by the atlas, such as the striatum.

The mean DS_c between the individual images and the template images is 0.90 ± 0.09.

As illustrated both by qualitatively and quantitatively, we could conclude that all these individual FDG-PET images, from different imaging centers and different subtypes of macaque, are normalized into the HJT space precisely.

3.4.2. Application the HJT in ischemic stroke studies

Comparing with healthy controls, the FDG-PET image of an ischemic stroke cynomolgus macaque was analyzed voxel-by-voxel (Table S3 and Fig. 7). As illustrated above and shown in Fig. 6B and C, there is a high degree of alignment between the healthy controls/stroke model and HJT set. The voxel-wised analysis results were presented in color-scaled superimposing on a 3D render surface of HJT using the BrainNet View toolkit (Xia et al., 2013), and axial slices of the structural image of a single macaque in HJT space, as shown in Fig. 7. The warm pseudo-color represented hyper-metabolic regions of ischemic stroke cynomolgus comparing with the healthy controls, while the cold pseudo-color stood for hypo-metabolic regions. Moreover, as illustrated in Table 1, the hypo-metabolic voxels located in the regions of the amygdala, motor cortex, prefrontal cortex, auditory cortex, entorhinal cortex and temporal cortex, which might be related to the ipsilesional infarction damage. The hyper-metabolic voxels were also observed in the prefrontal cortex and visual cortex of the contralesional hemisphere in the ischemic stroke cynomolgus compared with the healthy controls.

Table 1
The statistical results of two sample *t*-test between the ischemic stroke cynomolgus model and the 10 healthy controls.

Type	Anatomical Name	K_e	T_{max}	Stereotaxic coordinates		
				x	y	z
Hypo-metabolic regions	Amygdala	30	5.01	5.2	−1.2	13.5
	Motor cortex	49	5.62	21.2	−3.2	−12.5
	Prefrontal cortex	186	8.46	11.2	−26.2	−3.5
	Auditory cortex	24	5.22	26.2	1.8	2.5
	Entorhinal cortex	25	4.64	5.2	−0.2	14.5
	Temporal cortex	168	8.10	26.2	3.8	4.5
	Cerebellum	17	4.12	13.2	21.8	9.5
Hyper-metabolic regions	Prefrontal cortex	16	6.52	−1.8	−16.2	1.5
	Prefrontal cortex	66	5.32	1.2	3.8	−12.5
	Visual cortex	69	5.30	−8.8	40.8	−8.5

K_e: the size of a cluster, in which the number such as 30 stands for the voxel numbers in the cluster.
T_{max}: the maximum t-value in each cluster.
Stereotaxic coordinates: the coordinates of the maximum point in *Saleem and Logothetis atlas* space.
x: the x-axis, which is negative to the left and positive to the right.
y: the y-axis, which is negative to the Posterior and positive to the Anterior.
z: the z-axis, which is negative to the Superior and negative to the Inferior.

3.5. Constructed metabolic functional network

The constructed metabolic functional network of macaque was shown in hot maps (Fig. 8A) and in spatial topography surface (Fig. 8B). The detailed information of this modular network is listed in Table 2. We speculate from the modular network that most of the functional regions are bilaterally symmetric, especially in the basic functional regions. The modular No.3 was suspected as the basic functional network of the brain, which consists of bilateral auditory cortex, bilateral motor cortex, bilateral somatosensory cortex, bilateral visual cortex, bilateral cerebellum, bilateral cingulate, bilateral RSC, bilateral striatum, and bilateral DLPFC and VLPFC. These functional regions in modular No. 3 covers most of the body sensory and emotion. Moreover, the DLPFC and VLPFC are regarded as the endpoint for the dorsal pathway that indicates the brain how to interact with the stimuli (Knoch and Fehr, 2007). The modular No. 4 is more likely a typical audio-visual network, which is related with the fine motor movement. For example, a macaque is turning its head to the direction of the sound source (Roberts and Hall, 2008). Modular No. 1 and No. 2 are more likely correlated with higher cognitive functions, since the hippocampus plays a vital role in working memory (Cho et al., 2016), and the ectorhinal/entorhinal/hippocampus system is critical to particular

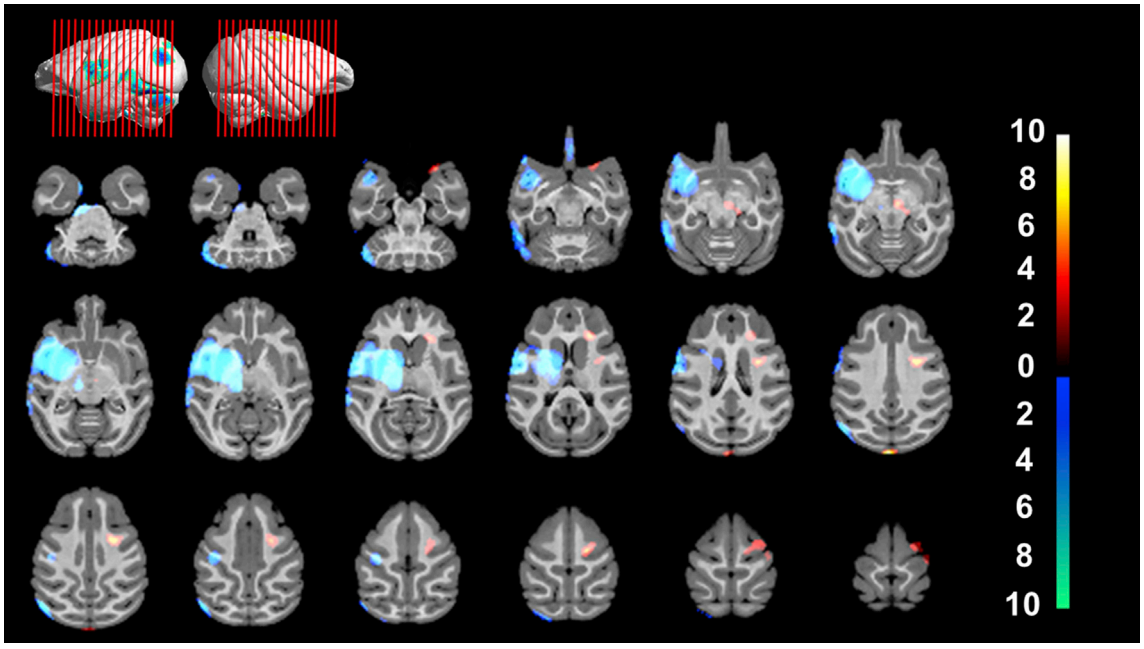

Fig. 7. Voxel-wised analysis result of FDG-PET images between a stroke cynomolgus model and a group of healthy controls (10 healthy cynomolgus). The statistical results were superimposed on a T1WI single brain in HJT space ($p < 0.05$, FDR correction, cluster > 20). The statistical results were shown in color-scaled, in which a warm pseudo-color indicated hyper-metabolic regions for stroke compared with healthy controls, while a cold pseudo-color represented hypo-metabolic regions. The T1WI single brain was shown in gray-scaled. The color bar stood for the t-value.

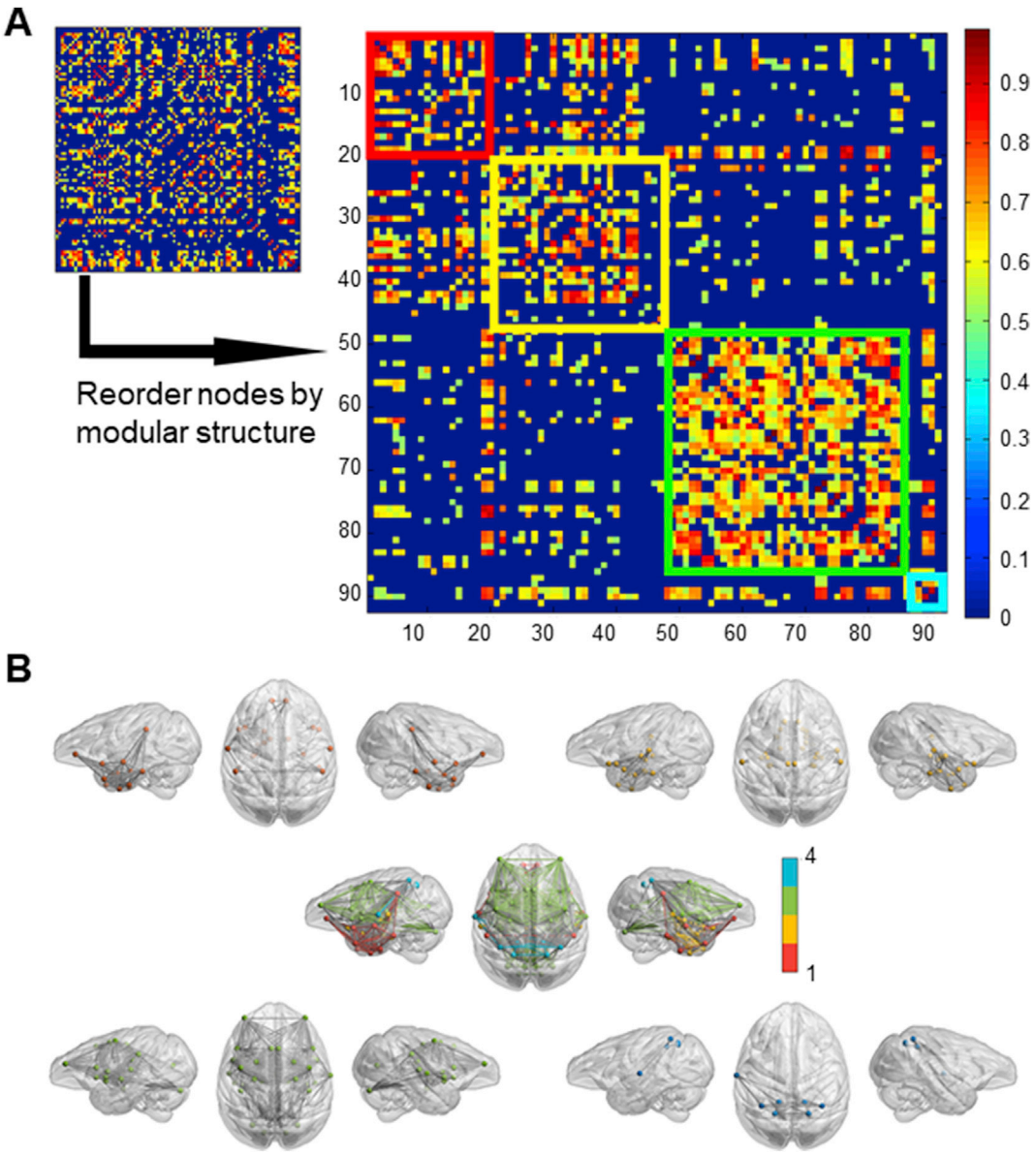

Fig. 8. The constructed metabolic functional network of the thirty healthy rhesus macaques for making template image. It is a sparse network that there are the least connections between these 82 functional regions. (A) The hot map of the network. The left one shows the original order of these 82 nodes, while the right one reorder the nodes by modular structure. These four modular are squared out in red, yellow, green and blue color. The color bar stands for the connection intensity between each pair of nodes. (B) The spatial topography map of the modular metabolic network overlaying on the surface of macaque in HJT space. These four modular are shown in different colors, and the modular color bar is shown in the middle. The whole network is shown in the middle, in which the modular No.1 is shown in red, No.2 is in yellow, No. 3 is in green and No.4 is in blue. The connections within a modular is in the same color with its corresponding node, while the connections between the modular is shown in gray. Each modular is shown at the four corners, in which the modular No.1 is on the upper left, No.2 is on the upper right, No.3 is at the bottom left, and No. 4 is at the bottom right.

spatial memory formation, memory consolidation and memory optimization during sleep.

4. Discussion

In the present study, a population stereotaxic template set of macaque brain named HJT was constructed for PET imaging studies. As an application example, it is further evaluated and applicated in data analysis of FDG-PET images of an ischemic stroke cynomolgus macaque (Chen et al., 2015a). This HJT was established on the widely used *Saleem and Logothetis atlas* space (Saleem and Logothetis, 2012), together with an elaborate delineated brain functional atlas. In addition, the HJT is compatible with the SPM and PMOD software, which is convenient for routine PET imaging data analysis.

A template set is preferably constructed from multi-subjects to possess brain anatomy population and greater cross-subject validity (Friston et al., 1999), such as the ICBM152 template for human brain studies which created from 152 subjects (Mazziotta et al., 2001). Therefore, in this study, our primary objective was to create an improved and representative population macaque brain template set as a standard reference in spatial normalization for PET neuroimaging studies from a large cohort of macaques. The population HJT was generated by iteratively registered and averaged using a validated template construction process (Mazziotta et al., 2001; Friston et al., 1999; Nie et al., 2013, 2014, 2019; Liang et al., 2017; Huang et al., 2018). As shown in Fig. 2, the boundary of anatomical regions in HJT is smooth, which is ideal for PET data analysis. Compared with previous studies that constructed PET template from only several monkeys (Collantes et al., 2009; Cross et al., 2000), the

Table 2
Detailed information of modular structure of the constructed metabolic functional network of the macaque as shown in Fig. 8.

Index	ROI name	Modular_Index
1	Amydala_L	1
2	Ectorhinal_cortex_L	1
3	Entorhinal_cortex_L	1
4	Hippocampus_L	1
5	Perirhinal_cortex_L	1
6	Perirhinal_cortex_R	1
7	Orbital_medial_prefrontal_cortex_L	1
8	Orbital_medial_prefrontal_cortex_R	1
9	Superior_temporal_gyrus_L	1
10	Superior_temporal_gyrus_R	1
11	Inferior_temporal_gyrus_L	1
12	Inferior_temporal_gyrus_R	1
13	Temporal_pole_L	1
14	Temporal_pole_R	1
15	Piriform_cortex_L	1
16	Piriform_cortex_R	1
17	Precentral_opercular_area_L	1
18	Precentral_opercular_area_R	1
19	Temporo-parietal_area_L	1
20	Temporo-parietal_area_R	1
21	Amydala_R	2
22	Auditory_cortex_core_areas_R	2
23	Ectorhinal_cortex_R	2
24	Entorhinal_cortex_R	2
25	Hippocampus_R	2
26	Parahippocampal_cortex_L	2
27	Parahippocampal_cortex_R	2
28	Dentate_gyrus_L	2
29	Dentate_gyrus_R	2
30	Globus_pallidus_L	2
31	Globus_pallidus_R	2
32	Lateral_geniculate_nucleus_L	2
33	Lateral_geniculate_nucleus_R	2
34	Olfactory _L	2
35	Olfactory _R	2
36	Retrosplenial_cortex_RSC_L	2
37	Retrosplenial_cortex_RSC_R	2
38	Auditory_cortex_core_areas_L	3
39	Auditory_cortex_lateral_areas_R	3
40	Auditory_cortex_medial_areas_L	3
41	Auditory_cortex_medial_areas_R	3
42	Cerebellum_L	3
43	Cerebellum_R	3
44	Claustrum_L	3
45	Claustrum_R	3
46	Dorsal_premotor_cortex_L	3
47	Dorsal_premotor_cortex_R	3
48	Insula_L	3
49	Insula_R	3
50	Primary_motor_cortex_L	3
51	Primary_motor_cortex _R	3
52	Dorsolateral_ prefrontal_cortex _L	3
53	Dorsolateral_ prefrontal_cortex _R	3
54	Ventrolateral_ prefrontal_cortex_L	3
55	Ventrolateral_ prefrontal_cortex_R	3
56	Striatum_caudate_L	3
57	Striatum_caudate_R	3
58	Striatum_putamen_L	3
59	Striatum_putamen_R	3
60	Ventral_premotor_cortex_L	3
61	Ventral_premotor_cortex_R	3
62	Cingulate_L	3
63	Cingulate_R	3
64	Gustatory_cortex_L	3
65	Gustatory_cortex_R	3
66	Mammillary_nucleus_L	3
67	Mammillary_nucleus_R	3
68	Motor_area_L	3
69	Motor_area_R	3
70	Secondary_somatosensory_area_L	3
71	Secondary_somatosensory_area_R	3
72	Somatosensory_areas_L	3
73	Somatosensory_areas_R	3
74	Occipital_cortex_L	3
75	Occipital_cortex_R	3
76	Auditory_cortex_lateral_areas_L	4
77	Parietal_cortex_posterior_L	4
78	Parietal_cortex_ posterior _R	4
79	Parietal_cortex_superior_L	4
80	Parietal_cortex_ superior_R	4
81	Parieto-occipital_area_L	4
82	Parieto-occipital_area_R	4

Index: The index number of all the functional regions shown in the reordered hot map of the metabolic network in Fig. 8A.
Modular_Index: The modular index in the spatial topography map of the metabolic network in Fig. 8B.

HJT showed substantial improvement in representation and validity.

PET imaging can visualize the distribution of biologically targeted radiotracers at the molecular level with high sensitivity. For example, the radiotracers are directly correlated with energy consumption that supports synaptic activities (Wang et al., 2016; Cheng et al., 2018), or pathogenesis as amyloid protein and tau-protein. In the receptor PET imaging studies, spatial normalization is always performed via MRI T1WI images named MRI-aided registration method. Therefore, an MRI T1WI template is always requisite in PET neuroimaging studies. Fig. 2A illustrated the creation of a population MRI T1WI structural template image in HJT. In previous studies, there are several structural templates of macaque with high spatial resolution that are beneficial to MRI studies (Black et al., 2001, 2004; McLaren et al., 2009; Quallo et al., 2010; Frey et al., 2011; Seidlitz et al., 2018; Reveley et al., 2017; Moirano et al., 2018). The *D99-SL* template, which was created from an *ex vivo* single-subject, has subtle sub-anatomical delineations (Reveley et al., 2017), while the NMT could identify the main blood vessels in macaque brain (Seidlitz et al., 2018). Both the template images have a high spatial resolution of 0.25 mm^3, while it is, however, nearly 2 mm^3 of a PET imaging. Using such a template, one single voxel in individual PET image could be interpolated to nearly 512 voxels when spatial normalization, which may introduce considerable deviation. Therefore, in light of the intrinsic lower spatial resolution of PET images, a new structural template of macaque has been created in HJT, which is smoother than previous template images. Moreover, the HJT is sharing a similar coordinate space with our newly constructed macaque brain atlas, which has 44 sub-functional regions (Saleem and Logothetis, 2012) and would be more frequently used in PET imaging studies.

Nowadays, FDG is the most commonly used radiotracer for PET investigation. Numerous studies have proven that the image registration accuracy is satisfactory when an image is registered to its corresponding imaging modality template (Meyer et al., 1999). Therefore, a specialized FDG-PET template image is also requisite in neuroimaging studies, not only in human brain studies (Friston et al., 1999) but also in animals (Cross et al., 2000; Nie et al., 2014; Huang et al., 2018). Recently, the population FDG-PET templates have been constructed for children (Uchiyama et al., 2013), treeshrew (Huang et al., 2018) and rat (Nie et al., 2014), while the latest version for macaque was created nearly twenty years ago based on only 6 FDG-PET images (Cross et al., 2000). Therefore, a population FDG-PET template is created in HJT, which is not only an improvement of previous studies but also a supplementary of MRI T1WI template.

The usage and accuracy of a newly created HJT were also evaluated in different studies. It was found that the spatial normalization of individual FDG-PET images to the HJT was satisfactory. Although these individual images were from different imaging centers, different subtypes of macaque, *i.e.* cynomolgus and rhesus, even a disease model, the accuracy of spatial normalization is stable. As illustrated by the qualitative evaluation results (Fig. 6), the segmentations of intercranial tissue, tissue class and sub-functional regions from the normalized individual images using

HJT, are all satisfactory. In addition, the laborious stripping extracranial tissues of individual images before spatial standardization is not necessary since the HJT processes both intracranial tissues and extracranial parts.

4.1. Application the HJT in voxel-wised single subject analysis

The number of animals in macaque imaging research is typically small, especially in disease model studies (Wang et al., 2016; Cheng et al., 2018), so that multi-subject analysis is limited. 3D-SSP (three-dimensional stereotactic surface projection) is a professional software in the single-subject analysis of PET images, which has self-contained healthy control database. Although the database is expensive, it is a pioneer in the single-subject analysis. Alternatively, SPM is also a powerful statistical analysis platform in neuroimaging studies, in which the single-to-multi comparisons are allowed (Acton and Friston, 1998). The baseline of healthy controls is defined by researches in SPM. With the HJT applying to SPM, single-subject analysis of macaque is effective. In this study, a single-subject voxel-wised analysis was performed on an ischemic stroke cynomolgus macaque (Chen et al., 2015a) compared with a group of healthy controls. The voxel-wised statistical result is shown in Fig. 7 and Table 1. The hypo-metabolic regions were mainly due to ischemia and edema, which was visualized in its original FDG-PET images. Compared with the control group, these obvious hypo-metabolic voxels of ischemic brain mainly lay in the ipsilesional hemisphere, consisting of motor cortex, prefrontal cortex, entorhinal cortex, amygdala, auditory cortex, temporal cortex and cerebellum, which is consistent with the previous research (Cai et al., 2009; Enzinger et al., 2009; Fu et al., 2009; Ivey et al., 2010). These hypo-metabolic regions contained not only the infarction areas, but also the edema and brain functional impairment areas, such as motor impairment. Among them, motor cortex, entorhinal cortex, amygdala, auditory cortex and cerebellum are known to be involved in orientation, motor skills, and sensory, which were proved to be relevant to stroke.

On the other hand, functional brain compensation also occurred in the stroke. As shown in Fig. 7 and Table 1, there were also several hypermetabolic regions. They were mainly located in the contralesional hemisphere, comprising with the prefrontal cortex and visual cortex. We suspected that these contralesional functional areas might supplement its corresponding contralateral lesion area similar to the previous studies. However, whether these functional supplementary acts as a negative role in prognosis recovery or not still needs further research.

4.2. Benefits from HJT in SUVR calculation

SUVR is one of the most commonly used semi-quantitative parameters in PET imaging studies (Chen et al., 2015b; Fleisher et al., 2013; Leinonen et al., 2014). One of the critical points in SUVR calculation is to choose an appropriate reference region. Up to now, the cerebellum, pons and white matter are the most commonly used reference regions (Chen et al., 2015b; Fleisher et al., 2013). Based on the TPM in HJT, the white matter is segmented out automatically using DARTEL algorithm (Mak et al., 2011), while the cerebellum or pons can be extracted based on the functional atlas image in HJT.

Another key point in SUVR calculation is ROI extraction. As the HJT is sharing a common space with previous studies (Seidlitz et al., 2018; Reveley et al., 2017), all the sub-anatomical structures, which is nearly one hundred, can be extracted easily from each individual via the HJT. Also, those 44 functional regions defined by HJT can be selected automatically. Moreover, the SUVR of these regions are calculated not only in the common space by normalization each individual into the HJT space, but also in individual space by transforming the HJT into each individual space (Nie et al., 2010). To demonstrate the utility of the HJT for calculating SUVR, the PET data of one rhesus brain were processed on the platform of SPM12 and PMOD (see Fig. S1 and Table S4 in Supporting Information), which showed similar results.

4.3. Compatibility of HJT with PMOD

Quantitative calculation of dynamic PET neuroimaging is regarded as a golden standard in the examination of in vivo pharmacokinetics of new radiotracers. Nowadays, the PMOD is the professional softwares in dynamic PET imaging analysis. To enable HJT widely-applicable in PET neuroimaging analysis, we incorporated our template with PMOD under the name 'Rhesus (IHEP_JNU)'. With the assistance of HJT in PMOD, the time-activity curve in each ROI of macaque brain can be conveniently and precisely analyzed, which serves as the output function of radiotracer for PET quantification.

4.4. Brain metabolic network construction based on HJT

Each functional brain region is not independent (Bullmore and Sporns, 2009; Schwarz et al., 2009). They are working as a dynamic network in handling different brain functions, such as motion, decision or cognition (Yeo et al., 2011). It is worthy of mentioning that the default mode network (DMN) of the human brain has been firstly disclosed by FDG-PET images (Gusnard et al., 2001). The metabolic network of brain function, constructed from the FDG-PET images, has been widely investigated in different neurological disorders (Tomse et al., 2017; Ma et al., 2015) as well as different species including human (Hu et al., 2015; Fang et al., 2016) and rodents (Lu et al., 2012; Choi et al., 2015; Hsu et al., 2016). Nowadays, the neurologic disease macaque models (i.e. autistic disorder) (Qiu, 2018) have been established and serves as valuable tools for translational studies. The FDG-PET brain metabolic functional network can be applied for the analysis of connections between different brain regions, facilitating a better understanding of brain sciences.

4.5. Application of HJT in multi-modality imaging studies

A set of population TPM is created in the HJT, which consists of three intracranial tissues such as GM, WM and CSF, as well as three extracranial parts including the skull, extracranial soft tissues and background (as shown in the Step a3 of Fig. 1). This TPM is compatible with SPM12. As we all known, the spatial normalization algorithm of human brain neuroimaging has been updated in the latest version of SPM - SPM12 (Acton and Friston, 1998). The most significant innovation entails the introduction of DARTEL algorithm, in which there are no multi-modality template images except a six-part TPM in MNI space of the human brain (Mazziotta et al., 2001; Friston et al., 1999). In the spatial normalization of SPM12, all the individual images, regardless their imaging modality, are firstly segmented into different tissues classes, and then the segmented individual's GM is normalized to the GM in TPM. Therefore, we could speculate that the HJT could be not only applied for PET studies of macaques, but also served as a general processing tool in multi-modality imaging data such as T1WI, functional MRI and arterial spin labeling images.

4.6. Limitations

There are also some limitations of this study. Firstly, the PET template was constructed based on the data acquired from clinical GE Discovery Elite 690 scanner, whose resolution is around 5 mm. This is applicable in the research community using comparable clinical scanners for macaque neuroimaging. For the PET images obtained from high resolution (<3 mm) scanners, our template still offers the advantage of providing a common, stereotactic space for group analysis, in which a spatial smoothing with ~4–6 mm is typically conducted. Also, using MRI-based partial volume correction to improve the spatial resolution of the PET is a potential direction for our further study. Secondly, only FDG-PET images were created in HJT, which may be unavailable for analysis of receptor PET imaging studies. We could speculate that individual MRI T1WI images can also be normalized with the HJT via MRI T1WI template accurately. Hence, for receptor PET imaging, the normalization accuracy

is mainly dependent on the co-registration precision between the PET and its corresponding T1WI images. In addition, as discussed in Section 4.5, we predicted that the TPM could be used in multi-modality neuroimaging analysis of the macaque brain. Although the FDG-PET images used in this study were normalized into the HJT space by TPM using DARTEL algorithm, we have found that the normalization accuracy of the stroke model was lower than others. Therefore, we speculated that the normalization accuracy is not satisfactory when the original individual images have noticeable lesions, such as ischemia and tumor. Besides, although the identification of regions with abnormal FDG uptake in the ischemic model was realized by the brain atlas in HJT, no comparisons against manually drawn ROI were conducted, which warrants further evaluation.

5. Conclusion

In conclusion, we have constructed a population stereotaxic HJT of macaque brain for PET neuroimaging data analysis, which is compatible with PMOD, SPM and other open-source, neuroimaging software packages. We believe that the HJT offers a unique tool to support research and collaborations across different institutions. The template would allow imaging scientists to study the structural and functional similarities between NHP and human, and improve our understanding of NHP brain via the establishment of such platform for data analysis and profiling.

Conflicts of interest

None.

Ethics statement

All applicable international, national, and institutional guidelines for the care and use of animals were followed. All procedures performed in studies involving animals were in accordance with the ethical standards of the Laboratory Animal Ethics Committee, Jinan University and its collaborative animal facility (Guangzhou), and/or Animal Care and Use Committee of the Chinese Academy of Sciences (Beijing), China. This article does not contain any studies with human performed by any of the authors.

Data availability statement

We claim that the FDG-PET and MRI T1 volume, segmentations, and surface representations in HJT would be openly available. Every nonprofit organization and research community could download HJT freely from the Supporting Information, and apply it to analyze macaque neuroimaging with citation of this article.

Acknowledgments

The authors would like to thank PET-BiO Technology and Landau Biotechnology for providing technical support in the animal experimental setup. We also thank Dr. Liow JS at NIMH for the helpful discussion, Mr. Guoping Yin (Enhanced Application Specialist, China Application Team, GE Healthcare) for optimizing MRI sequences for macaque brain images. This work was financially supported by the National Natural Science Foundation of China (81671770, 81701751, 81871383, 81771923), the Strategic Priority Research Program of Chinese Academy of Science (XDB32030200), the Science and Technology Program of Guangzhou (201804010440), the Shenzhen Basic Research Program (JCYJ20160330095629781), and the Fundamental Research Funds for the Central Universities (21617311, 21619104). The authors report no conflicts of interest.

Appendix A. Supplementary data

Supplementary data to this article can be found online at https://doi.org/10.1016/j.neuroimage.2019.116163.

References

Acton, P.D., Friston, K.J., 1998. Statistical parametric mapping in functional neuroimaging: beyond PET and fMRI activation studies. Eur. J. Nucl. Med. 25, 663–667.

Alessio, A.M., Kinahan, P.E., Lewellen, T.K., 2006. Modeling and incorporation of system response functions in 3-D whole body PET. IEEE Trans. Med. Imaging 25, 828–837.

Black, K.J., Koller, J.M., Snyder, A.Z., Perlmutter, J.S., 2001. Template images for nonhuman primate neuroimaging: 2. Macaque. Neuroimage 14, 744–748. https://doi.org/10.1006/nimg.2001.0871.

Black, K.J., Koller, J.M., Snyder, A.Z., Perlmutter, J.S., 2004. Atlas template images for nonhuman primate neuroimaging: baboon and macaque. Methods Enzymol. 385, 91–102. https://doi.org/10.1016/S0076-6879(04)85006-7.

Bullmore, E., Sporns, O., 2009. Complex brain networks: graph theoretical analysis of structural and functional systems. Nat. Rev. Neurosci. 10, 186–198. https://doi.org/10.1038/nrn2575.

Cai, W., Guzman, R., Hsu, A.R., Wang, H., Chen, K., Sun, G., et al., 2009. Positron emission tomography imaging of poststroke angiogenesis. Stroke 40, 270–277. https://doi.org/10.1161/STROKEAHA.108.517474.

Chae, S.Y., Kim, H.O., Oh, M., Lee, D.Y., Jin, S., Oh, S.J., et al., 2014. Evaluation of selective positron emission tomography template method for spatial normalization of amyloid imaging with 11C-Pittsburgh Compound B. J. Comput. Assist. Tomogr. 38, 924–929. https://doi.org/10.1097/RCT.0000000000000123.

Chai, P., Feng, B., Zhang, Z., Tang, H., Liu, S., Sun, X., et al., 2019. NEMA NU-4 performance evaluation of a non-human primate animal PET. Phys. Med. Biol. https://doi.org/10.1088/1361-6560/ab1614.

Chen, X., Dang, G., Dang, C., Liu, G., Xing, S., Chen, Y., et al., 2015. An ischemic stroke model of nonhuman primates for remote lesion studies: a behavioral and neuroimaging investigation. Restor. Neurol. Neurosci. 33, 131–142. https://doi.org/10.3233/RNN-140440.

Chen, K., Roontiva, A., Thiyyagura, P., Lee, W., Liu, X., Ayutyanont, N., et al., 2015. Improved power for characterizing longitudinal amyloid-beta PET changes and evaluating amyloid-modifying treatments with a cerebral white matter reference region. J. Nucl. Med. 56, 560–566. https://doi.org/10.2967/jnumed.114.149732.

Cheng, R., Mori, W., Ma, L., Alhouayek, M., Hatori, A., Zhang, Y., et al., 2018. Vitro and in vivo evaluation of (11)C-labeled azetidinecarboxylates for imaging monoacylglycerol lipase by PET imaging studies. J. Med. Chem. 61, 2278–2291. https://doi.org/10.1021/acs.jmedchem.7b01400.

Chiotis, K., Saint-Aubert, L., Rodriguez-Vieitez, E., Leuzy, A., Almkvist, O., Savitcheva, I., et al., 2018. Longitudinal changes of tau PET imaging in relation to hypometabolism in prodromal and Alzheimer's disease dementia. Mol. Psychiatry 23, 1666–1673. https://doi.org/10.1038/mp.2017.108.

Cho, H., Choi, J.Y., Hwang, M.S., Lee, J.H., Kim, Y.J., Lee, H.M., et al., 2016. Tau PET in Alzheimer disease and mild cognitive impairment. Neurology 87, 375–383. https://doi.org/10.1212/WNL.0000000000002892.

Choi, H., Choi, Y., Kim, K.W., Kang, H., Hwang, D.W., Kim, E.E., et al., 2015. Maturation of metabolic connectivity of the adolescent rat brain. Elife 4. https://doi.org/10.7554/eLife.11571.

Collantes, M., Prieto, E., Penuelas, I., Blesa, J., Juri, C., Marti-Climent, J.M., et al., 2009. New MRI, 18F-DOPA and 11C-(+)-alpha-dihydrotetrabenazine templates for Macaca fascicularis neuroimaging: advantages to improve PET quantification. Neuroimage 47, 533–539. https://doi.org/10.1016/j.neuroimage.2009.04.078.

Cross, D.J., Minoshima, S., Nishimura, S., Noda, A., Tsukada, H., Kuhl, D.E., 2000. Three-dimensional stereotactic surface projection analysis of macaque brain PET: development and initial applications. J. Nucl. Med. 41, 1879–1887.

Enzinger, C., Dawes, H., Johansen-Berg, H., Wade, D., Bogdanovic, M., Collett, J., et al., 2009. Brain activity changes associated with treadmill training after stroke. Stroke 40, 2460–2467. https://doi.org/10.1161/STROKEAHA.109.550053.

Fang, L., Yao, Z., An, J., Chen, X., Xie, Y., Zhao, H., et al., 2016. Topological organization of metabolic brain networks in pre-chemotherapy cancer with depression: a resting-state PET study. PLoS One 11, e0166049. https://doi.org/10.1371/journal.pone.0166049.

Fleisher, A.S., Chen, K., Liu, X., Ayutyanont, N., Roontiva, A., Thiyyagura, P., et al., 2013. Apolipoprotein E epsilon4 and age effects on florbetapir positron emission tomography in healthy aging and Alzheimer disease. Neurobiol. Aging 34, 1–12. https://doi.org/10.1016/j.neurobiolaging.2012.04.017.

Frey, S., Pandya, D.N., Chakravarty, M.M., Bailey, L., Petrides, M., Collins, D.L., 2011. An MRI based average macaque monkey stereotaxic atlas and space (MNI monkey space). Neuroimage 55, 1435–1442. https://doi.org/10.1016/j.neuroimage.2011.01.040.

Friston, K.J., 1995. Commentary and opinion: II. Statistical parametric mapping: ontology and current issues. J. Cereb. Blood Flow Metab. 15, 361–370. https://doi.org/10.1038/jcbfm.1995.45.

Friston, K.J., Holmes, A.P., Price, C.J., Buchel, C., Worsley, K.J., 1999. Multisubject fMRI studies and conjunction analyses. Neuroimage 10, 385–396. https://doi.org/10.1006/nimg.1999.0484.

Fu, Y.K., Chang, C.J., Chen, K.Y., Hwang, L.C., Wu, K.H., Chang, K.W., et al., 2009. Imaging of regional metabolic activity by (18)F-FDG/PET in rats with transient cerebral ischemia. Appl. Radiat. Isot. 67, 1743–1747. https://doi.org/10.1016/j.apradiso.2009.03.002.

Gusnard, D.A., Raichle, M.E., Raichle, M.E., 2001. Searching for a baseline: functional imaging and the resting human brain. Nat. Rev. Neurosci. 2, 685–694. https://doi.org/10.1038/35094500.

Gutierrez, D.F., Zaidi, H., 2012. Automated analysis of small animal PET studies through deformable registration to an atlas. Eur. J. Nucl. Med. Mol. Imaging 39, 1807–1820. https://doi.org/10.1007/s00259-012-2188-7.

Hsu, L.M., Liang, X., Gu, H., Brynildsen, J.K., Stark, J.A., Ash, J.A., et al., 2016. Constituents and functional implications of the rat default mode network. Proc. Natl. Acad. Sci. U. S. A. 113, E4541–E4547. https://doi.org/10.1073/pnas.1601485113.

Hu, Y., Xu, Q., Shen, J., Li, K., Zhu, H., Zhang, Z., et al., 2015. Small-worldness and gender differences of large scale brain metabolic covariance networks in young adults: a FDG PET study of 400 subjects. Acta Radiol. 56, 204–213. https://doi.org/10.1177/0284185114529106.

Huang, Q., Nie, B., Ma, C., Wang, J., Zhang, T., Duan, S., et al., 2018. Stereotaxic (18)F-FDG PET and MRI templates with three-dimensional digital atlas for statistical parametric mapping analysis of tree shrew brain. J. Neurosci. Methods 293, 105–116. https://doi.org/10.1016/j.jneumeth.2017.09.006.

Ivey, F.M., Hafer-Macko, C.E., Ryan, A.S., Macko, R.F., 2010. Impaired leg vasodilatory function after stroke: adaptations with treadmill exercise training. Stroke 41, 2913–2917. https://doi.org/10.1161/STROKEAHA.110.599977.

Knoch, D., Fehr, E., 2007. Resisting the power of temptations: the right prefrontal cortex and self-control. Ann. N. Y. Acad. Sci. 1104, 123–134. https://doi.org/10.1196/annals.1390.004.

Leinonen, V., Rinne, J.O., Wong, D.F., Wolk, D.A., Trojanowski, J.Q., Sherwin, P.F., et al., 2014. Diagnostic effectiveness of quantitative [(1)(8)F]flutemetamol PET imaging for detection of fibrillar amyloid beta using cortical biopsy histopathology as the standard of truth in subjects with idiopathic normal pressure hydrocephalus. Acta Neuropathol. Commun. 2, 46. https://doi.org/10.1186/2051-5960-2-46.

Liang, S., Wu, S., Huang, Q., Duan, S., Liu, H., Li, Y., et al., 2017. Rat brain digital stereotaxic white matter atlas with fine tract delineation in Paxinos space and its automated applications in DTI data analysis. Magn. Reson. Imaging 43, 122–128. https://doi.org/10.1016/j.mri.2017.07.011.

Lu, H., Zou, Q., Gu, H., Raichle, M.E., Stein, E.A., Yang, Y., 2012. Rat brains also have a default mode network. Proc. Natl. Acad. Sci. U. S. A. 109, 3979–3984. https://doi.org/10.1073/pnas.1200506109.

Ma, Y., Johnston, T.H., Peng, S., Zuo, C., Koprich, J.B., Fox, S.H., et al., 2015. Reproducibility of a Parkinsonism-related metabolic brain network in non-human primates: a descriptive pilot study with FDG PET. Mov. Disord. 30, 1283–1288. https://doi.org/10.1002/mds.26302.

Mak, H.K., Zhang, Z., Yau, K.K., Zhang, L., Chan, Q., Chu, L.W., 2011. Efficacy of voxel-based morphometry with DARTEL and standard registration as imaging biomarkers in Alzheimer's disease patients and cognitively normal older adults at 3.0 Tesla MR imaging. J. Alzheimer's Dis. 23, 655–664. https://doi.org/10.3233/JAD-2010-101659.

Mazziotta, J., Toga, A., Evans, A., Fox, P., Lancaster, J., Zilles, K., et al., 2001. A probabilistic atlas and reference system for the human brain: international Consortium for Brain Mapping (ICBM). Philos. Trans. R. Soc. Lond. B Biol. Sci. 356, 1293–1322. https://doi.org/10.1098/rstb.2001.0915.

McLaren, D.G., Kosmatka, K.J., Oakes, T.R., Kroenke, C.D., Kohama, S.G., Matochik, J.A., et al., 2009. A population-average MRI-based atlas collection of the rhesus macaque. Neuroimage 45, 52–59. https://doi.org/10.1016/j.neuroimage.2008.10.058.

Meyer, J.H., Gunn, R.N., Myers, R., Grasby, P.M., 1999. Assessment of spatial normalization of PET ligand images using ligand-specific templates. Neuroimage 9, 545–553. https://doi.org/10.1006/nimg.1999.0431.

Moirano, J.M., Bezgin, G.Y., Ahlers, E.O., Kotter, R., Converse, A.K., 2018. Rhesus macaque brain atlas regions aligned to an MRI template. Neuroinformatics. https://doi.org/10.1007/s12021-018-9400-2.

Nie, B., Hui, J., Wang, L., Chai, P., Gao, J., Liu, S., et al., 2010. Automatic method for tracing regions of interest in rat brain magnetic resonance imaging studies. J. Magn. Reson. Imaging 32, 830–835. https://doi.org/10.1002/jmri.22283.

Nie, B., Chen, K., Zhao, S., Liu, J., Gu, X., Yao, Q., et al., 2013. A rat brain MRI template with digital stereotaxic atlas of fine anatomical delineations in paxinos space and its automated application in voxel-wise analysis. Hum. Brain Mapp. 34, 1306–1318. https://doi.org/10.1002/hbm.21511.

Nie, B., Liu, H., Chen, K., Jiang, X., Shan, B., 2014. A statistical parametric mapping toolbox used for voxel-wise analysis of FDG-PET images of rat brain. PLoS One 9, e108295. https://doi.org/10.1371/journal.pone.0108295.

Nie, B., Liang, S., Jiang, X., Duan, S., Huang, Q., Zhang, T., et al., 2018. An automatic method for generating an unbiased intensity normalizing factor in positron emission tomography image analysis after stroke. Neurosci. Bull. 34, 833–841. https://doi.org/10.1007/s12264-018-0240-8.

Nie, B., Wu, D., Liang, S., Liu, H., Sun, X., Li, P., et al., 2019. A stereotaxic MRI template set of mouse brain with fine sub-anatomical delineations: application to MEMRI studies of 5XFAD mice. Magn. Reson. Imaging 57, 83–94. https://doi.org/10.1016/j.mri.2018.10.014.

Popescu, V., Battaglini, M., Hoogstrate, W.S., Verfaillie, S.C., Sluimer, I.C., van Schijndel, R.A., et al., 2012. Optimizing parameter choice for FSL-Brain Extraction Tool (BET) on 3D T1 images in multiple sclerosis. Neuroimage 61, 1484–1494. https://doi.org/10.1016/j.neuroimage.2012.03.074.

Qiu, Z., 2018. Deciphering MECP2-associated disorders: disrupted circuits and the hope for repair. Curr. Opin. Neurobiol. 48, 30–36. https://doi.org/10.1016/j.conb.2017.09.004.

Quallo, M.M., Price, C.J., Ueno, K., Asamizuya, T., Cheng, K., Lemon, R.N., et al., 2010. Creating a population-averaged standard brain template for Japanese macaques (M. fuscata). Neuroimage 52, 1328–1333. https://doi.org/10.1016/j.neuroimage.2010.05.006.

Rapisarda, E., Bettinardi, V., Thielemans, K., Gilardi, M.C., 2010. Image-based point spread function implementation in a fully 3D OSEM reconstruction algorithm for PET. Phys. Med. Biol. 55, 4131–4151. https://doi.org/10.1088/0031-9155/55/14/012.

Reveley, C., Gruslys, A., Ye, F.Q., Glen, D., Samaha, J., B, E.R., et al., 2017. Three-dimensional digital template Atlas of the macaque brain. Cerebr. Cortex 27, 4463–4477. https://doi.org/10.1093/cercor/bhw248.

Roberts, K.L., Hall, D.A., 2008. Examining a supramodal network for conflict processing: a systematic review and novel functional magnetic resonance imaging data for related visual and auditory stroop tasks. J. Cogn. Neurosci. 20, 1063–1078. https://doi.org/10.1162/jocn.2008.20074.

Rohlfing, T., Kroenke, C.D., Sullivan, E.V., Dubach, M.F., Bowden, D.M., Grant, K.A., et al., 2012. The INIA19 template and NeuroMaps atlas for primate brain image parcellation and spatial normalization. Front. Neuroinf. 6, 27. https://doi.org/10.3389/fninf.2012.00027.

Saleem, K.S., Logothetis, N.K., 2012. A Combined MRI and Histology Atlas of the Rhesus Monkey Brain in Stereotaxic Coordinates, second ed. Elsevier/Academic press with Horizontal, Coronal and Sagittal series, San Diego.

Schwarz, A.J., Gozzi, A., Bifone, A., 2009. Community structure in networks of functional connectivity: resolving functional organization in the rat brain with pharmacological MRI. Neuroimage 47, 302–311. https://doi.org/10.1016/j.neuroimage.2009.03.064.

Seidlitz, J., Sponheim, C., Glen, D., Ye, F.Q., Saleem, K.S., Leopold, D.A., et al., 2018. A population MRI brain template and analysis tools for the macaque. Neuroimage 170, 121–131. https://doi.org/10.1016/j.neuroimage.2017.04.063.

Tomse, P., Jensterle, L., Rep, S., Grmek, M., Zaletel, K., Eidelberg, D., et al., 2017. The effect of 18F-FDG-PET image reconstruction algorithms on the expression of characteristic metabolic brain network in Parkinson's disease. Phys. Med. 41, 129–135. https://doi.org/10.1016/j.ejmp.2017.01.018.

Tzourio-Mazoyer, N., Landeau, B., Papathanassiou, D., Crivello, F., Etard, O., Delcroix, N., et al., 2002. Automated anatomical labeling of activations in SPM using a macroscopic anatomical parcellation of the MNI MRI single-subject brain. Neuroimage 15, 273–289. https://doi.org/10.1006/nimg.2001.0978.

Uchiyama, H.T., Seki, A., Tanaka, D., Koeda, T., Jcs, G., 2013. A study of the standard brain in Japanese children: morphological comparison with the MNI template. Brain Dev. 35, 228–235. https://doi.org/10.1016/j.braindev.2012.04.005.

Van Essen, D.C., Glasser, M.F., Dierker, D.L., Harwell, J., 2012. Cortical parcellations of the macaque monkey analyzed on surface-based atlases. Cerebr. Cortex 22, 2227–2240. https://doi.org/10.1093/cercor/bhr290.

Wang, J., Wang, X., Xia, M., Liao, X., Evans, A., He, Y., 2015. GRETNA: a graph theoretical network analysis toolbox for imaging connectomics. Front. Hum. Neurosci. 9 https://doi.org/10.3389/fnhum.2015.00386, 386.

Wang, L., Mori, W., Cheng, R., Yui, J., Hatori, A., Ma, L., et al., 2016. Synthesis and preclinical evaluation of sulfonamido-based [(11)C-Carbonyl]-Carbamates and ureas for imaging monoacylglycerol lipase. Theranostics 6, 1145–1159. https://doi.org/10.7150/thno.15257.

Xia, M., Wang, J., He, Y., 2013. BrainNet Viewer: a network visualization tool for human brain connectomics. PLoS One 8, e68910. https://doi.org/10.1371/journal.pone.0068910.

Yeo, B.T., Krienen, F.M., Sepulcre, J., Sabuncu, M.R., Lashkari, D., Hollinshead, M., et al., 2011. The organization of the human cerebral cortex estimated by intrinsic functional connectivity. J. Neurophysiol. 106, 1125–1165. https://doi.org/10.1152/jn.00338.2011.

Zhang, Y.P., Shi, L.M., 1993. Phylogeny of rhesus monkeys (Macaca mulatta) as revealed by mitochondrial DNA restriction enzyme analysis. Int. J. Primatol. 14, 587–605. https://doi.org/10.1007/BF02215449.

Zhang, T., Huang, Q., Jiao, C., Liu, H., Nie, B., Liang, S., et al., 2019. Modular architecture of metabolic brain network and its effects on the spread of perturbation impact. Neuroimage 186, 146–154. https://doi.org/10.1016/j.neuroimage.2018.11.003.